



Cite this: *Nanoscale Adv.*, 2020, **2**, 4557

Synthesis of Zn-based 1D and 2D coordination polymer nanoparticles in block copolymer micelles†

Christoph Göbel,^a Gerald Hörner,^a Andreas Greiner,^a Holger Schmalz^{a,b} and Birgit Weber^a

Nanoparticles of the 1D and 2D coordination polymers $[\text{Zn}(\text{OAc})_2(\text{bipy})]_n$ and $[\text{Zn}(\text{TFA})_2(\text{bppa})_2]_n$ were prepared, employing polystyrene-*block*-poly(4-vinylpyridine) diblock copolymers with different weight fractions of the 4-vinylpyridine (4VP) block and comparable overall molecular weights of $M_n \approx 155 \text{ kg mol}^{-1}$ as template (SV-15 and SV-42 with 15 and 42 wt% 4VP, respectively). $[\text{Zn}(\text{OAc})_2(\text{bipy})]_n$ nanoparticles were successfully synthesised within the 4VP core of SV-42 micelles, showing a core size of $D_{\text{core}} = 47 \pm 5 \text{ nm}$ and a hydrodynamic diameter of $D_h = 157 \pm 46 \text{ nm}$, determined by transmission electron microscopy (TEM) and dynamic light scattering (DLS). The crystallinity of the composite is quite low, showing only low intensity reflexes in the powder X-ray diffraction (PXRD) pattern with the highest particle load. No indications for larger microcrystals were detected by scanning electron microscopy (SEM), proving the successful integration of the coordination polymer nanoparticles within the micellar cores. Nanocomposites of the 2D coordination network $[\text{Zn}(\text{TFA})_2(\text{bppa})_2]_n$ were synthesised using both diblock copolymers. The particle core sizes (from TEM) and hydrodynamic diameters (from DLS) correlate with the 4VP fraction of the micelles, resulting in $D_{\text{core}} = 46 \pm 6 \text{ nm}$ for SV-42 and $15 \pm 2 \text{ nm}$ for SV-15 and $D_h = 340 \pm 153 \text{ nm}$ and $177 \pm 57 \text{ nm}$, respectively. The successful synthesis was proven by PXRD and SEM images, confirming the absence of larger crystallites. Hence, it is possible to synthesise nanocomposites of Zn-based 1D and 2D coordination polymers by a direct approach utilizing diblock copolymer micelles as template.

Received 26th April 2020
Accepted 5th September 2020

DOI: 10.1039/d0na00334d

rsc.li/nanoscale-advances

Introduction

Devices built up from functional molecular materials are an interesting approach to realize new functionalities for new fields of applications. Examples for promising molecule-based systems are porous coordination networks (MOFs, metal organic frameworks), Prussian blue based materials or molecular magnetic materials including spin crossover coordination polymers.^{1–9} Nanoparticles and nanocomposites of such materials are often considered to play a key role in future device engineering.^{10–15} However, the synthesis of well-defined, stable nanoparticles or nanocomposites of molecule-based materials is a highly demanding task, as a wide range of techniques successfully used for solid state materials (e.g. the reduction of

metal salts^{16–20} or the hydrothermal synthesis^{21–23}) are inapplicable. For molecular materials, some synthetic procedures like the inverse micelle technique^{24–28} or micro-fluidic approaches using fast precipitation^{29–31} have already been established to achieve that task. However, each new material has its needs regarding the reaction conditions (e.g. reaction temperature, solvent, reactant solubility, air or moisture sensitivity). Furthermore, some of the approaches have limitations regarding the size limits that can be reached. This makes a fine-tuning of the reaction conditions indispensable to not only achieve a successful synthesis of the nanomaterial of the desired size, but also to preserve the desired properties. Furthermore, some synthesis procedures have been proven more suitable for the formation of functional materials than others, because they allow for example the even distribution of the nanomaterial or nanocomposite on surfaces or prevent the aggregation of the formed nanoparticles.^{32,33}

Nanoparticles of 2D^{34–36} or 3D^{24,37,38} coordination networks (CNs) have been prepared with a wide range of bridging ligands and metal ions. However, the formation of 2D and 3D CN nanoparticles directly in the core of block copolymer micelles is quite rare. To the best of our knowledge, only 6 examples of 2D or 3D CN nanoparticles formed in a polymer matrix can be

^aDepartment of Chemistry, Inorganic Chemistry IV, Universität Bayreuth, Universitätsstraße 30, 95447 Bayreuth, Germany. E-mail: weber@uni-bayreuth.de

^bDepartment of Chemistry, Macromolecular Chemistry II, Keylab Synthesis and Molecular Characterization, Bavarian Polymer Institute, Universität Bayreuth, Universitätsstraße 30, 95447 Bayreuth, Germany. E-mail: holger.schmalz@uni-bayreuth.de

† Electronic supplementary information (ESI) available. See DOI: [10.1039/d0na00334d](https://doi.org/10.1039/d0na00334d)



found in the literature.^{39–44} A more commonly used technique is the immobilization of pre-formed nanoparticles in block copolymer micelles or polymer matrices (bulk polymers, gels, etc.),^{45–55} in some cases even size-selective employing polymer cages.⁵⁶

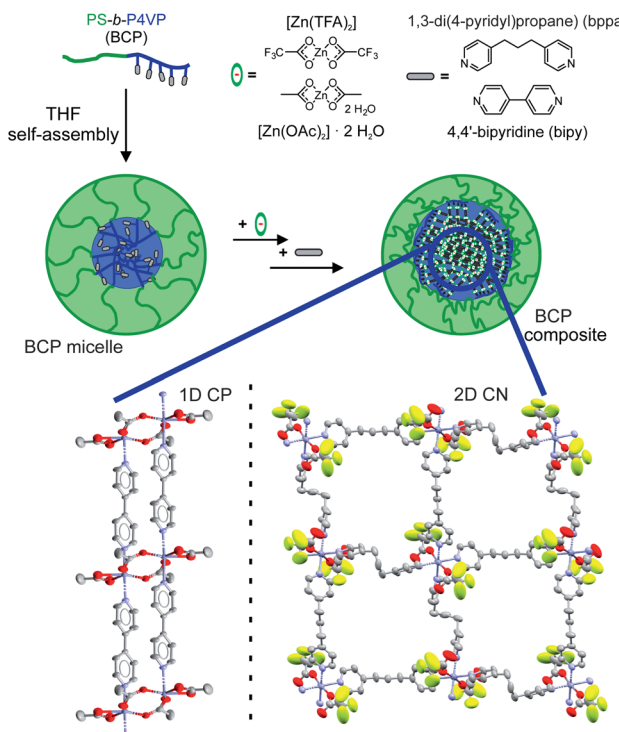
We have previously shown that the use of polystyrene-*block*-poly(4-vinylpyridine) (PS-*b*-P4VP) diblock copolymers (BCPs) is ideal for the size-controlled synthesis of 1D Fe(n) spin crossover (SCO) coordination polymer (CP) nanoparticles with core sizes of 16 ± 2 nm and 48 ± 4 nm. It was possible to retain the SCO properties with hysteresis at both particle sizes. Thermal treatment of the 16 nm particles triggers a confined crystallization of the NPs leading to SCO properties comparable to those of the bulk material.^{57,58} In other cases, the synthesis in confinement results in different morphologies for NPs and bulk material and therefore different SCO properties.⁵⁹

Herein, we report the successful adaptation of our general synthetic concept to a completely new type of CPs and for the first time to a 2D CN to illustrate its general applicability. The double-stranded 1D CP $[\text{Zn}(\text{OAc})_2(\text{bipy})]_n$ ⁶⁰ (bipy = 4,4'-bipyridine) and the layer-like 2D CN $[\text{Zn}(\text{TFA})_2(\text{bppa})_2]_n$ ⁶¹ (TFA = trifluoroacetic acid, bppa = 1,3-di(4-pyridyl)propane) were used for the formation of Zn-CP/CN-BCP nanocomposites. The nanocomposites were synthesised using two PS-*b*-P4VP diblock copolymers (SV-15 and SV-42) as templates, which have an almost identical molecular weight but differ in the weight fraction of the 4VP blocks (see Table 1).

Results and discussion

Synthetic procedures

The synthesis procedure was adapted from the literature and adjusted to the requirements of the Zn-based CPs (Scheme 1).⁵⁸ Dissolving the diblock copolymer in THF leads to the formation of BCP micelles due to the significantly lower solubility of the P4VP block compared to the PS block. Thus the less-soluble P4VP core, where the synthesis of the NPs takes place, is surrounded by soluble PS corona chains. The nanocomposite samples containing the 1D CP $[\text{Zn}(\text{OAc})_2(\text{bipy})]_n$ were synthesised employing SV-42 diblock copolymer micelles in THF (Table 2). The Zn(II) precursor $[\text{Zn}(\text{OAc})_2] \cdot 2\text{H}_2\text{O}$ was added and the solution was refluxed for 1 h. Subsequently, the solution was cooled down, the bridging ligand bipy was added and the



Scheme 1 Synthetic approach for the preparation of Zn-based CP-BCP nanocomposites. An excerpt of the crystal structures of both CP bulk materials is given below (left: $[\text{Zn}(\text{OAc})_2(\text{bipy})]_n$, right: $[\text{Zn}(\text{TFA})_2(\text{bppa})_2]_n$).

solution was refluxed again for 1 h. At this point, the synthesis can be stopped by removal of the solvent *via* rotary evaporation (sample 1; 1 cycle) or $[\text{Zn}(\text{OAc})_2] \cdot 2\text{H}_2\text{O}$ and bipy can be added simultaneously up to 4 more times (samples 2–4; 3–5 cycles). The resulting light-yellow solids were dried *in vacuo*.

The BCPs SV-15 and SV-42 were used for the synthesis of nanocomposites containing the 2D CN $[\text{Zn}(\text{TFA})_2(\text{bppa})_2]_n$ (Table 2). Here, the synthesis protocol had to be adapted due to the very low solubility of the desired 2D CN. The respective BCPs were dissolved under reflux in THF to trigger the self-assembly to micelles, $[\text{Zn}(\text{TFA})_2] \cdot \text{H}_2\text{O}$ was added and the mixture was heated to reflux for 1 h to initiate the coordination of the zinc(II) precursor at the pyridine units in the P4VP core of the micelle.

Table 1 Overview of the used BCPs in this work

BCP	M_n^a [g mol ⁻¹]	D^b	PS : P4VP ^c [w/w]	D_{core}^d [nm]	D_{h}^e [nm]
SV-15	154 000	1.02	85 : 15	15 ± 2	75 ± 28
SV-42	157 000	1.09	58 : 42	45 ± 5	125 ± 34

^a Calculated from proton nuclear magnetic resonance (¹H NMR) measurements, using the molecular weight of the PS precursor measured by matrix-assisted laser desorption-time of flight mass spectrometry (MALDI-ToF MS). ^b From gel permeation chromatography (GPC) in *N,N*-dimethylformamide using narrowly distributed PS standards for calibration. ^c Calculated from ¹H NMR measurements. ^d Core diameters of empty BCP micelles, see Fig. S1 for TEM images and core size distributions. ^e Hydrodynamic diameters of the empty BCP micelles, see Fig. S2 for DLS measurements.

Table 2 Overview of the synthesised nanocomposites

Sample	CP/CN	BCP	Cycles	D_{core}^a [nm]	D_{h}^b [nm]
1	$[\text{Zn}(\text{OAc})_2(\text{bipy})]_n$	SV-42	1	50 ± 4	141 ± 48
2			3	47 ± 4	155 ± 42
3			4	47 ± 4	152 ± 41
4			5	47 ± 5	157 ± 46
5	$[\text{Zn}(\text{TFA})_2(\text{bppa})_2]_n$	SV-15	1	13 ± 1	139 ± 39
6		SV-42	1	49 ± 4	160 ± 46
7		SV-15	2	15 ± 2	177 ± 57
8		SV-42	2	46 ± 6	340 ± 153

^a Core diameters of the nanocomposite particles (determined by TEM).

^b Hydrodynamic diameters of the nanocomposite particles (determined by DLS).



To avoid a precipitation of the CN and to decelerate its formation, the bridging ligand bppa was dissolved in THF and added dropwise to the reaction solution over 15 min, followed by a 1 h reflux. The solvent was removed by rotary evaporation and subsequent drying *in vacuo* to yield light-yellow samples **5** and **6** (1 cycle each). The reaction procedure can be repeated to yield samples **7** and **8** (2 cycles each) with a higher complex loading. The formation of nanocomposites with higher cycle counts (>2) was tested, but the formation of microcrystals was observed by SEM (see Fig. S3†). Therefore, no further addition of reactants was conducted after the second addition of bppa (for experimental details see Experimental section).

Characterisation of nanocomposites

In total, eight different nanocomposites have been synthesised (Table 2), of which four contain the 1D CP $[\text{Zn}(\text{OAc})_2(\text{bipy})]_n$ (samples **1–4**) and another four the 2D CN $[\text{Zn}(\text{TFA})_2(\text{bpppa})_2]_n$ (samples **5–8**). All nanocomposite materials were characterised by transmission electron microscopy (TEM) and dynamic light scattering (DLS) to evaluate the particle sizes in the dry state and in dispersion. Furthermore, the nanocomposites were analysed by elemental analysis (C, H, N), infrared spectroscopy (IR), powder X-ray diffraction (PXRD), and scanning electron microscopy (SEM). IR measurements were supported by computational calculations.

$[\text{Zn}(\text{OAc})_2(\text{bipy})]_n$ nanocomposites

IR measurements of the starting material $[\text{Zn}(\text{OAc})_2] \cdot 2\text{H}_2\text{O}$, the bulk material $[\text{Zn}(\text{OAc})_2(\text{bipy})]_n$ and the samples **1–4** are displayed in Fig. 1A. The nanocomposites show a characteristic band at 1598 cm^{-1} , which increases in intensity relative to other bands when higher cycle counts are reached. This is in excellent agreement with the spectrum of independently synthesised bulk $[\text{Zn}(\text{OAc})_2(\text{bipy})]_n$, which features a band at 1600 cm^{-1} . Thus, this band can be safely assigned to the C=O stretching mode of the neat CP. Peak assignment in the fingerprint area between 1400 cm^{-1} and 1800 cm^{-1} proved valuable to identify the nature and purity of the nanocomposites, which was further supported by numerical frequency calculations of optimized

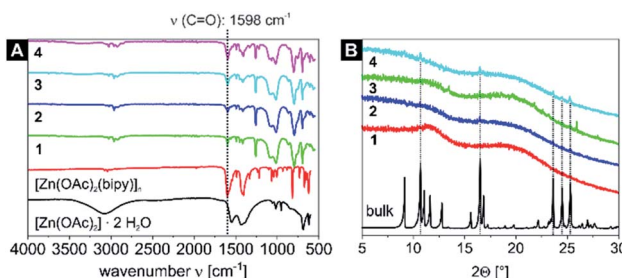


Fig. 1 IR spectra of the starting material $[\text{Zn}(\text{OAc})_2] \cdot 2\text{H}_2\text{O}$, the CP $[\text{Zn}(\text{OAc})_2(\text{bipy})]_n$ and the four $[\text{Zn}(\text{OAc})_2(\text{bipy})]_n$ nanocomposite samples **1–4** (A) and a comparison of the PXRD patterns of the bulk material $[\text{Zn}(\text{OAc})_2(\text{bipy})]_n$ and the $[\text{Zn}(\text{OAc})_2(\text{bipy})]_n$ nanocomposite samples **1–4** (B). PXRD reflexes that correlate with the bulk material are marked with a dashed line.

model structures. The CP was approximated as binuclear $[\text{Zn}_2(\text{OAc})_4(\text{py})_4]$, whereas the H-bond network of the precursor was taken into account in pentanuclear $[\text{Zn}(\text{OAc})_2(\text{OH}_2)] \times 4 [\text{Zn}(\text{OAc})_2(\text{OH}_2)]$ (see Experimental section for computational details, animations of diagnostic modes are given in the ESI,† anim_1–6). In fact, the calculated C=O stretching mode in the CP model $[\text{Zn}_2(\text{OAc})_2(\text{py})_2]_n$ is located at 1601 cm^{-1} , almost identical to samples **1–4** and the bulk material. This is a distinct difference to the C=O band of the precursor $[\text{Zn}(\text{OAc})_2] \cdot 2\text{H}_2\text{O}$, which is experimentally found at 1549 cm^{-1} (computed value: 1534 cm^{-1}). The formation of single-stranded $[\text{Zn}(\text{OAc})_2(\text{bipy})]_n$ can be similarly ruled out, as C=O based stretching modes computed for the model $[\text{Zn}(\text{OAc})_2(\text{py})_2]$ are predicted at 1500 cm^{-1} , proving the successful synthesis of the 1D CP in the P4VP core of the SV-42 micelles.

Further proof is given by the PXRD patterns of the samples **1–4**. Samples **1–3** are highly amorphous as indicated by the powder diffraction patterns. Only sample **4** with five reaction cycles shows five reflexes that also correspond to the dominant reflexes of the bulk material (Fig. 1B) indicating a successful formation of the CP inside the micellar core.

Exemplary for all nanocomposites with the $[\text{Zn}(\text{OAc})_2(\text{bipy})]_n$ CP, the TEM and DLS measurements of sample **4** are displayed in Fig. 2. The corresponding core diameter and hydrodynamic diameter of all samples are summarized in Table 2. The DLS measurement shows narrowly distributed nanocomposite particles with a hydrodynamic diameter of $D_h = 157 \pm 46\text{ nm}$. As the electron-rich $[\text{Zn}(\text{OAc})_2(\text{bipy})]_n$ CP is incorporated inside the micelle core of the BCP, only the core of nanocomposite particles is clearly visible in TEM, resulting in notably smaller diameters compared to DLS. The TEM image of sample **4** shows spherical particle cores with a core size of $D_{\text{core}} = 47 \pm 5\text{ nm}$ (Fig. 2). In line with the results for other coordination polymers reported so far,^{57–59} particles core sizes and hydrodynamic diameters of samples **1–3** are nearly identical and slightly increased compared to the empty template. Respective data of

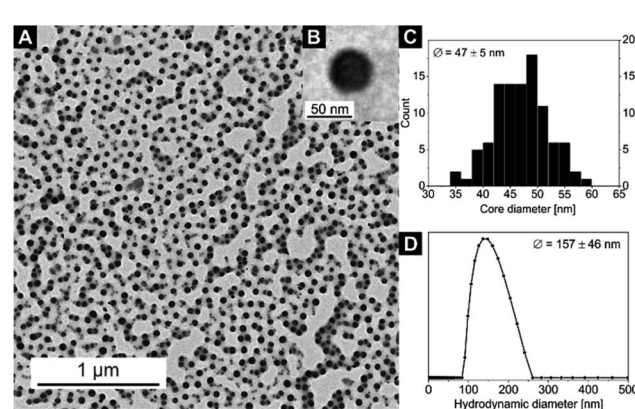


Fig. 2 (A) TEM image of sample **4**, the cores of the micelles with the embedded $[\text{Zn}(\text{OAc})_2(\text{bipy})]_n$ CP nanoparticles appear black, (B) an inset with a zoom on a single nanoparticle, (C) core size distribution D_{core} (from TEM) and (D) hydrodynamic diameter distribution D_h (from DLS) of the nanocomposite sample **4** (for DLS autocorrelation function see Fig. S6†).



all samples confirming these results can be found in Fig. S4 and S5† together with the autocorrelation function of sample 4 (Fig. S6†).

The samples **1–4** were also characterised by SEM, revealing the absence of microcrystals on the sample surface (Fig. S7†). Thus, the CN is regioselectively formed inside the cores of the BCP micelles.

[Zn(TFA)₂(bppa)₂]_n nanocomposites

IR measurements were also performed for the four nanocomposites containing the [Zn(TFA)₂(bppa)₂]_n CN (samples **5–8**, Fig. 3A and S8†) and were compared to the starting material [Zn(TFA)₂]_·H₂O and the bulk material [Zn(TFA)₂(bppa)₂]_n. The starting material shows a C=O band at 1695 cm⁻¹ with a shoulder at 1715 cm⁻¹, whereas the bulk CN shows two characteristic bands in the range of C=O vibrations at 1698 cm⁻¹ and 1681 cm⁻¹. Computation of a truncated mononuclear model of the CN, [Zn(TFA)₂(py)₄], similarly gives two bands at 1668 cm⁻¹ and 1662 cm⁻¹. For samples **5–7** only one band was detected at 1690 cm⁻¹, which is exactly between the two bands of the bulk CN. For sample **8** two bands for the CN were determined at 1699 cm⁻¹ and 1684 cm⁻¹, being in good agreement with the bulk material. Again, a relative increase in intensity of the carbonyl band is detectable with higher cycles. Thus, it was possible to incorporate the 2D CN into the 4VP cores of both micellar templates (SV-15 and SV-42). In line with the PXRD results of the [Zn(OAc)₂(bipy)]_n CP nanocomposites, the samples **5** and **6** (one loading cycle) are completely amorphous as represented by the diffraction patterns. Nevertheless, samples **7** and **8** (two loading cycles) already show some reflexes at positions that match with the bulk material, indicating the successful formation of the desired CN inside the BCP micelles (Fig. 3B).

Particle sizes of the nanocomposites were also analysed by TEM and DLS (Fig. 4, 5; S9–S11†). While sample **5** only shows spherical particles with core sizes of $D_{\text{core}} = 13 \pm 1$ nm (Fig. S9†), sample **7** shows spherical particles which, however, tend to form chain-like aggregates (Fig. 4). This behaviour was

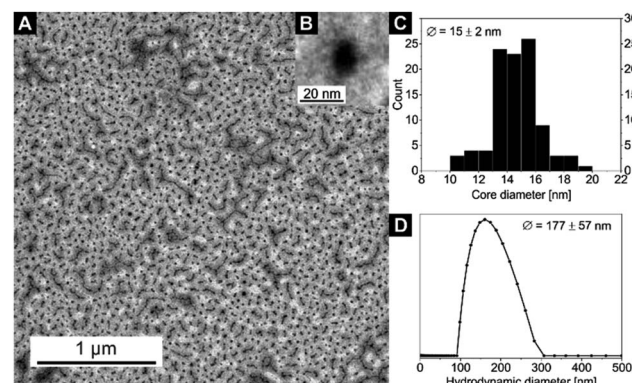


Fig. 4 (A) TEM image of sample 7. (B) An inset with a zoom on a single nanoparticle. (C) Core size distribution D_{core} (from TEM) and (D) hydrodynamic diameter distribution D_h (from DLS) of nanocomposite sample 7 (for DLS autocorrelation function see Fig. S11†).

also observed in other samples of the same nanocomposite (Fig. S12†). In fact, the formation of spherical particles rather than worm-like micelles in THF would be expected in THF due to the low 4VP fraction of the utilised SV-15 diblock copolymer.^{62,63} The presence of the anisotropic 2D CN together with the limited space available in the P4VP core of the highly asymmetric SV-15 BCP micelles ($D_{\text{core}} = 15 \pm 2$ nm, $D_h = 177 \pm 57$ nm for sample 7) could trigger the formation of chain-like structures, even at comparably low 4VP fractions. This may be an effect that occurs during drying of the sample on the TEM grid, since the hydrodynamic diameter distribution of sample 7 is rather narrow (Fig. 4C) and D_h is only slightly increased compared to that of sample 5 (Table 2).

The particle core sizes of samples **6** ($D_{\text{core}} = 49 \pm 4$ nm, Fig. S9†) and **8** ($D_{\text{core}} = 46 \pm 6$ nm, Fig. 5) are in good agreement with the core sizes of samples **1–4** ($D_{\text{core}} \approx 47$ –50 nm, Fig. 2 and S4†), which were synthesised using the same BCP (SV-42, Table 2). This underlines the fact that the BCP determines the size of the nanocomposites. Again, the formed nanocomposite particles tend to form chain-like structures for sample **8** (2 loading

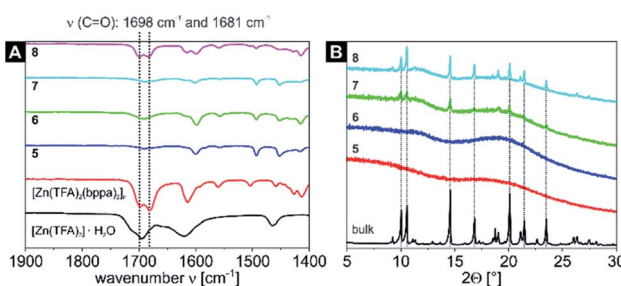


Fig. 3 Detailed view on the spectral range of 1900 cm⁻¹ to 1400 cm⁻¹ of the IR spectra of the starting material [Zn(TFA)₂]_·H₂O, the CN [Zn(TFA)₂(bppa)₂]_n, and the four [Zn(TFA)₂(bppa)₂]_n nanocomposite samples **5–8** (A). The complete spectra can be found in Fig. S8†. Comparison of the PXRD patterns of the bulk material [Zn(TFA)₂(bppa)₂]_n and the [Zn(TFA)₂(bppa)₂]_n nanocomposite samples **5–8** (B). Most intense PXRD reflexes that correlate with the bulk material are marked with a dashed line.

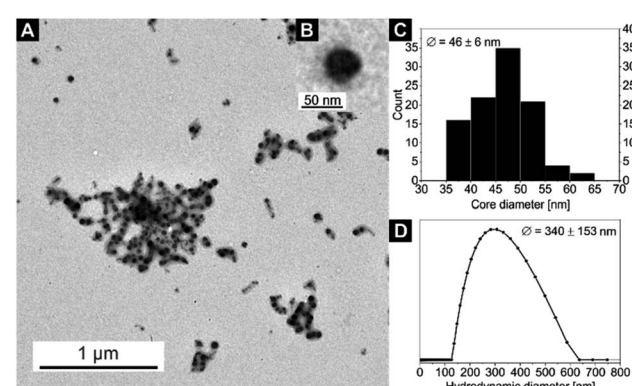


Fig. 5 (A) TEM image of sample 8. (B) An inset with a zoom on a single nanoparticle. (C) Core size distribution D_{core} (from TEM) and (D) hydrodynamic diameter distribution D_h (from DLS) of sample 8 (for DLS autocorrelation function see Fig. S11†).



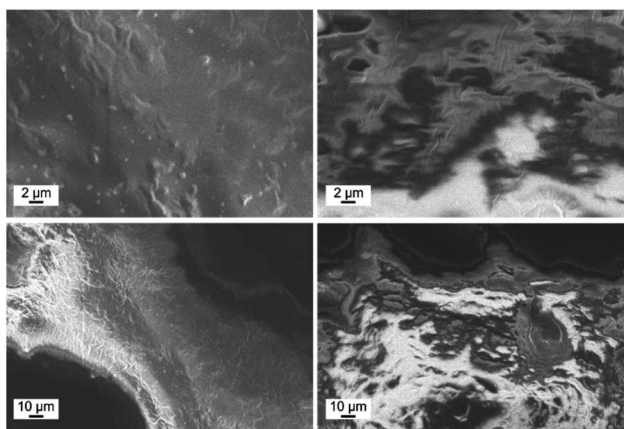


Fig. 6 SEM images of sample 7 (left) and sample 8 (right) at two different magnifications. No microcrystals can be observed on the polymer surface for both samples.

cycles), as observed by TEM. Another interesting phenomenon arises upon comparing the DLS measurements of samples **6** and **8**. While the average hydrodynamic diameter of sample **6** was determined to $D_h = 160 \pm 46$ nm (Fig. S10†), which correlates well with the hydrodynamic diameters of the samples **1–4**, the average hydrodynamic diameter of sample **8** is more than twice as large ($D_h = 340 \pm 153$ nm, Fig. 5) and the hydrodynamic diameter distribution is significantly broadened. This might point to the presence of chain-like (worm-like) structures already in solution. The shorter soluble PS blocks in the corona of SV-42 micelles might be less efficient in shielding the highly anisotropic CN in the micellar core and, thus, favouring the formation of chain-like structures. This assumption is supported by the fact that in Fig. 5A individual spherical CN nanoparticles can be recognized in the chain-like micellar structures.

The SEM images for the samples **5–8** (Fig. 6, and S13†) show the absence of microcrystals at the surface of the nanocomposites, proving that the 2D CN is incorporated inside the P4VP cores of the BCP micelles. However, if samples with more than 2 reaction cycles were synthesised, the very low solubility of the 2D CN $[\text{Zn}(\text{TFA})_2(\text{bpppa})_2]_n$ led to a fast precipitation of the CN, thus, resulting in the formation of microcrystals on the polymer surface and in the reaction solution. Consequently, the formation of truncated cuboctahedron crystals on the nanocomposite surface was observed by SEM (Fig. S3†).

Conclusions

The synthesis of well-defined 1D, 2D and 3D coordination polymer (CP) and network (CN) nanoparticles is highly challenging. Self-assembled polymeric micelles derived from block copolymers (BCPs) that offer coordination sites inside the micellar core may be an elegant and generally applicable concept for the direct synthesis of these CP and CN nanoparticles (NPs). We were able to show that our established synthetic approach can be adapted to other 1D CP like the double-stranded $[\text{Zn}(\text{OAc})_2(\text{bipy})]_n$ and more importantly to the

2D CN $[\text{Zn}(\text{TFA})_2(\text{bpppa})_2]_n$. Employing micelles of the BCP SV-42 as template it was possible to achieve spherical NPs of the 1D CP $[\text{Zn}(\text{OAc})_2(\text{bipy})]_n$ and the 2D CN $[\text{Zn}(\text{TFA})_2(\text{bpppa})_2]_n$ with nanocomposite core sizes of $D_{\text{core}} = 47 \pm 5$ nm and $D_{\text{core}} = 46 \pm 6$ nm, respectively. The average hydrodynamic diameter was determined to $D_h = 157 \pm 46$ nm for the $[\text{Zn}(\text{OAc})_2(\text{bipy})]_n$ and to $D_h = 340 \pm 153$ nm for the $[\text{Zn}(\text{TFA})_2(\text{bpppa})_2]_n$ nanocomposites. Moreover, even smaller composite NPs of the 2D CN $[\text{Zn}(\text{TFA})_2(\text{bpppa})_2]_n$ were successfully prepared in SV-15 micelles, having a core size D_{core} as small as 15 ± 2 nm and a hydrodynamic diameter of $D_h = 139 \pm 39$ nm. No microcrystals were found on the nanocomposite surface as proven by SEM measurements. The crystallinity of the nanocomposite samples increases with the loading cycles, showing characteristic reflexes in the PXRD at positions identical to the bulk materials. Since it was possible to synthesise NPs of the double-stranded 1D CP $[\text{Zn}(\text{OAc})_2(\text{bipy})]_n$ and particularly the 2D CN $[\text{Zn}(\text{TFA})_2(\text{bpppa})_2]_n$, we are convinced that our synthetic approach can be adapted to a wide range of other 1D, 2D, and even 3D CP and CN nanoparticles, which will be investigated in future work.

Experimental section

Materials

4,4'-Bipyridine (bipy, 98%), 1,3-di(4-pyridyl)propane (bpppa, 98%) and $[\text{Zn}(\text{OAc})_2] \cdot 2\text{H}_2\text{O}$ (97+%) were obtained from Alfa Aesar and used as received. For the synthesis of $[\text{Zn}(\text{TFA})_2] \cdot \text{H}_2\text{O}$, zinc oxide (ZnO , 99.9%) from Sigma Aldrich, trifluoroacetic acid (TFA, 99%) from Alfa Aesar and ethanol (EtOH, p.a., Fisher Chemical) were used as received. Tetrahydrofuran (THF, p.a.) was obtained from Fisher Chemical and used as received in the synthesis of the coordination polymers and the nanocomposites.

The two polystyrene-*block*-poly(4-vinylpyridine) diblock copolymers (SV-15 and SV-42) were synthesised by sequential anionic polymerization of styrene and 4-vinylpyridine according to our previously published method.⁵⁷

For gel permeation chromatography (GPC) in *N,N*-dimethylformamide (DMF) with lithium bromide (5 g L⁻¹), GRAM columns (300 × 8 mm, 10 μm particle size, PSS Mainz) with 100 and 3000 Å pore sizes were used. The samples were measured on a SEC 1260 Infinity system (Agilent Technologies) at a flow rate of 0.5 mL min⁻¹ at 23 °C, using a refractive index detector (Agilent Technologies). The calibration was done with narrowly distributed polystyrene standards (PSS calibration kit) and toluene (HPLC grade) was used as internal standard.

MALDI-ToF MS (matrix-assisted laser desorption/ionization time-of-flight mass spectrometry) measurements were performed on a Reflex III (Bruker) equipped with a N₂ Laser ($\lambda = 337$ nm). An acceleration voltage of 20 kV was used in linear mode and the samples were prepared according to the dried droplet method. Matrix (*trans*-2-[3-(4-*tert*-butylphenyl)-2-methyl-2-propenylidene]malononitrile, DCTB, 10 g L⁻¹ in THF), analyte (10 g L⁻¹ in THF) and salt (silver trifluoroacetate, 10 g L⁻¹ in THF) were dissolved and mixed in the ratio of 20 : 5 : 1 and 0.5 μL of the mixture was placed and dried on the target plate.



¹H-NMR spectra were acquired with a Bruker Ultrashield 300 spectrometer using CDCl₃ as solvent.

Transmission electron microscopy (TEM) was conducted on a Zeiss CEM902 electron microscope (Zeiss, Oberkochen, Germany). Samples were dispersed in THF at a concentration of 2 g L⁻¹. The unfiltered solution was dropped on a carbon coated copper grid (mesh 200, Science Services, Munich). Electron acceleration voltage was set to 80 kV. Micrographs were taken with a MegaView III/iTEM image acquiring and processing system from Olympus Soft Imaging Systems (OSIS, Münster, Germany) and an Orius 830 SC200W/DigitalMicrograph system from Gatan (Munich, Germany). Particles size measurements were done with "ImageJ" image processing software developed by Wayne Rasband (National Institutes of Health, USA).

Scanning electron microscopy (SEM) micrographs were taken on a Zeiss LEO 1530 GEMINI. The acceleration voltage was set to 3 kV and the sample was sputter-coated with a 1.3 nm platinum layer.

Dynamic light scattering (DLS) measurements were done with an AntonPaar Litesizer 500 in quartz glass cuvettes from Helma at 25 °C in backscattering mode (175°). One measurement consists of six consecutive runs. Samples were dispersed in THF at a concentration of 2 g L⁻¹. The unfiltered solution was used. A cumulant fit was used for fitting the experimental data.

Room temperature powder X-ray diffraction (PXRD) data were collected with a STOE StadiP X-ray diffractometer in transmission geometry between 5° and 30° 2θ for all samples, which were placed on flat surfaces. Cu-*K*_{α1} radiation ($\lambda = 1.541$ Å) was used for the measurements together with a Mythen 1K detector.

For elemental analysis, the carbon, nitrogen and hydrogen contents were determined with a Vario EL III (Elementar Analysensysteme GmbH) with acetanilide as standard or at a Uni-cube (Elementar Analysensysteme GmbH) with sulfanilamide as standard. The samples were placed in tin boats and measured at least twice. The average of the measurements was used.

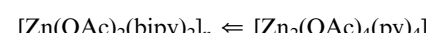
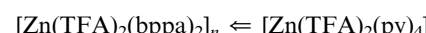
Transmission infrared spectra (IR) were collected on a Perkin Elmer Spectrum 100 FT-IR (ATR). The samples were measured directly as solids.

Computation setting

Theoretical structure calculations on the zinc(II) precursor complexes and coordination polymer/network models have been performed through density-functional theory (DFT) methods using the ORCA program package.⁶⁴ For all optimizations triple-ξ-valence TZVP⁶⁵ basis sets were used with the generalized gradient approximated functional BP86.⁶⁶ Grimme's third generation D3 correction of dispersion was used.^{67,68} Medium effects were included in a dielectric continuum approach (COSMO), parameterized for acetonitrile;⁶⁹ the inclusion of a stationary dielectric background proved beneficial for the match between experimental and theoretically observed structures. Optimized structures have been identified as stationary points through the absence of imaginary modes in harmonic frequency calculations; spurious

low-frequency imaginary modes in some calculations due to -CH₃ rotations are typical artefacts of DFT-based numerical frequency scans. Coordinates of the computed structures are assembled in the ESI, Tables S1–S4.[†] Graphical presentation of the vibrational modes are also available (anim_1–6.gif).

Phenomenological approach. The input structure of [Zn(TFA)₂(OH₂)₄] was extracted from the available XRD data.⁷⁰ In order to reduce computational cost, we have approximated the coordination polymers and the bulk [Zn(OAc)₂]·2H₂O precursor as truncated model complexes. Thereby we have put emphasis on the conservation of the first coordination sphere of the zinc centres. The bidentate bridging ligands were mimicked as monodentate pyridine ligands. In particular we employed the settings:



The highly H-bonded nature of the molecular modules in [Zn(OAc)₂]·2H₂O made it necessary to extract a pentanuclear motif from the crystal structure. Herein the central module possesses a conserved H-bond network (C=O and coordinated water) to serve as the theoretical probe; H-bond donor and acceptor sites of the terminal modules remained unsaturated. As a matter of fact, this model gives very satisfying agreement with the experimental IR spectrum. Graphical representations of the DFT optimized structure models are given in the ESI, Fig. S14 and S15.[†]

Synthesis

Synthesis of [Zn(TFA)₂]·H₂O. [Zn(TFA)₂]·H₂O was synthesised by dissolving 1 g (12.3 mmol, 1 eq.) ZnO in 10 mL EtOH and 1.9 mL (2.8 g, 24.6 mmol, 2 eq.) TFA in an ice bath and stirred until complete dissolution. The solution was filtered and the solvent was evaporated on a heating plate at 120 °C for several days. The resulting white powder was transferred into a Schlenk flask, dried *in vacuo* and stored under argon. Yield: 3.42 g (11.7 mmol, 90%). Elemental anal. (%) calc: C 16.49, H 0.65, found: C 16.51, H 0.70.

Synthesis of [Zn(OAc)₂(bipy)]_n nanocomposites (samples 1–4). 50 mg of the diblock copolymer SV-42 were placed and dissolved in a 50 mL flask in 20 mL THF under reflux until complete dissolution. The polymer solution was cooled down to rt, 2.2 mg (10 µmol, 1 eq.) [Zn(OAc)₂]·2H₂O were added and the solution was refluxed for 1 h. Subsequently, the reaction mixture was cooled down to rt and 2.4 mg (15 µmol, 1.5 eq.) 4,4'-bipyridine were added to the solution which was refluxed again for 1 h. At this point, the synthesis can be stopped by removal of the solvent by rotary evaporation to obtain sample 1 (1 cycle). Alternatively, 2.2 mg [Zn(OAc)₂]·2H₂O and 2.4 mg 4,4'-bipyridine can be added simultaneously up to 4 more times (samples 2–4; 3–5 cycles). All resulting light yellow solids were dried *in vacuo*.

Elemental anal. (%) found:



Sample 1: C 68.85, H 7.96, N 4.17.
 Sample 2: C 65.98, H 7.06, N 4.50.
 Sample 3: C 68.61, H 6.92, N 5.38.
 Sample 4: C 71.02, H 6.67, N 5.68.

Synthesis of $[\text{Zn}(\text{TFA})_2(\text{bppa})_2]_n$ nanocomposites (samples 5–8)

50 mg of the diblock copolymer SV-15 were placed in a 50 mL flask fitted with a magnetic stir bar. 20 mL THF were added and the polymer was dissolved under reflux until complete dissolution. The polymer solution was cooled down to rt and 2.0 mg (6.5 μmol , 1 eq.) $[\text{Zn}(\text{TFA})_2] \cdot \text{H}_2\text{O}$ were added and the solution was refluxed again for 1 h. Subsequently, the reaction solution was cooled down to rt. 2.8 mg (14 μmol , 2.2 eq.) 1,3-di(4-pyridyl)propane (bppa) were dissolved in 10 mL THF and the solution was added dropwise over 15 min. After the addition of the ligand solution, the reaction mixture was refluxed again for 1 h. The synthesis can be stopped by removal of the solvent by rotary evaporation to obtain sample 5 (1 cycle). Alternatively, the synthesis procedure can be repeated exactly as before to synthesise sample 7 (2 cycles). The resulting light yellow solids were dried *in vacuo*.

Besides the adjustment of the reactants, the synthetic procedure for samples 6 and 8 using the diblock copolymer SV-42 is identical to samples 5 and 7, respectively. 5.8 mg (19 μmol , 1 eq.) $[\text{Zn}(\text{TFA})_2] \cdot \text{H}_2\text{O}$ and 8.3 mg (42 μmol , 2.2 eq.) 1,3-di(4-pyridyl)propane were used during the synthesis.

Elemental anal. (%) found:

Sample 5: C 84.08, H 7.66, N 2.42.
 Sample 6: C 70.81, H 8.26, N 4.82.
 Sample 7: C 67.24, H 7.36, N 2.64.
 Sample 8: C 64.40, H 7.02, N 5.05.

Conflicts of interest

There are no conflicts to declare.

Acknowledgements

Financial support of the University of Bayreuth and the SFB 840 (TP A10 and A2) is gratefully acknowledged. Christoph Göbel was supported by the BayNAT program of the University of Bayreuth. We acknowledge the Keylab Electron and Optical Microscopy of the Bavarian Polymer Institute for providing access to the electron microscopy facilities (SEM and TEM). We thank Magdalena Weber, Thomas Bindig and Samanta Jänsch for their contribution to the synthesis of the composites and the bulk materials, as well as Florian Puchtler (Inorganic Chemistry I, University of Bayreuth) for PXRD, Dr Christine Denner (Inorganic Chemistry II, University of Bayreuth) for SEM and Rika Schneider (Macromolecular Chemistry II, University of Bayreuth) for GPC measurements.

Notes and references

1 T. Kitao, Y. Zhang, S. Kitagawa, B. Wang and T. Uemura, Hybridization of MOFs and polymers, *Chem. Soc. Rev.*, 2017, **46**, 3108–3133.

2 E. Coronado, Molecular magnetism: from chemical design to spin control in molecules, materials and devices, *Nat. Rev. Mater.*, 2020, **5**, 87–104.

3 K. Senthil Kumar, Y. Bayeh, T. Gebretsadik, F. Elemo, M. Gebrezgiabher, M. Thomas and M. Ruben, Spin-crossover in iron(II)-Schiff base complexes, *Dalton Trans.*, 2019, **48**, 15321–15337.

4 J. Calbo, M. J. Golomb and A. Walsh, Redox-active metal-organic frameworks for energy conversion and storage, *J. Mater. Chem. A*, 2019, **7**, 16571–16597.

5 T. Rodenas, I. Luz, G. Prieto, B. Seoane, H. Miro, A. Corma, F. Kapteijn, F. X. Llabrés i Xamena and J. Gascon, Metal-organic framework nanosheets in polymer composite materials for gas separation, *Nat. Mater.*, 2015, **14**, 48–55.

6 P. Horcajada, T. Chalati, C. Serre, B. Gillet, C. Sebrie, T. Baati, J. F. Eubank, D. Heurtaux, P. Clayette, C. Kreuz, J.-S. Chang, Y. K. Hwang, V. Marsaud, P.-N. Bories, L. Cynober, S. Gil, G. Férey, P. Couvreur and R. Gref, Porous metal-organic-framework nanoscale carriers as a potential platform for drug delivery and imaging, *Nat. Mater.*, 2010, **9**, 172–178.

7 X. Roy, J. K.-H. Hui, M. Rabnawaz, G. Liu and M. J. MacLachlan, Prussian blue nanocontainers, *J. Am. Chem. Soc.*, 2011, **133**, 8420–8423.

8 M. Ohba, K. Yoneda, G. Agustí, M. C. Muñoz, A. B. Gaspar, J. A. Real, M. Yamasaki, H. Ando, Y. Nakao, S. Sakaki and S. Kitagawa, Bidirectional chemo-switching of spin state in a microporous framework, *Angew. Chem., Int. Ed.*, 2009, **48**, 4767–4771.

9 E. A. Flügel, A. Ranft, F. Haase and B. V. Lotsch, Synthetic routes toward MOF nanomorphologies, *J. Mater. Chem.*, 2012, **22**, 10119–10133.

10 *Nanoparticle technology handbook*, ed. K. Hosokawa, K. Nogi, M. Naitō and T. Yokoyama, Elsevier, Amsterdam, Netherlands, 2018.

11 D. J. Harding, in *Novel Magnetic Nanostructures*, ed. E. Rentschler, N. Domracheva and M. Caporali, Elsevier, [S.l.], 2018, pp. 401–426.

12 L. Salmon and L. Catala, Spin-crossover nanoparticles and nanocomposite materials, *C. R. Chim.*, 2018, **21**, 1230–1269.

13 S. Rat, M. Piedrahita-Bello, L. Salmon, G. Molnár, P. Demont and A. Bousseksou, Coupling Mechanical and Electrical Properties in Spin Crossover Polymer Composites, *Adv. Mater.*, 2018, **30**, 1705275.

14 K. Otsubo, T. Haraguchi and H. Kitagawa, Nanoscale crystalline architectures of Hofmann-type metal-organic frameworks, *Coord. Chem. Rev.*, 2017, **346**, 123–138.

15 K. Senthil Kumar and M. Ruben, Emerging trends in spin crossover (SCO) based functional materials and devices, *Coord. Chem. Rev.*, 2017, **346**, 176–205.

16 Y. Sun and Y. Xia, Shape-controlled synthesis of gold and silver nanoparticles, *Science*, 2002, **298**, 2176–2179.

17 A. Henglein, Colloidal Palladium Nanoparticles: Reduction of Pd(II) by H₂; Pd Core Au Shell Ag Shell Particles, *J. Phys. Chem. B*, 2000, **104**, 6683–6685.

18 H. Wang, X. Qiao, J. Chen and S. Ding, Preparation of silver nanoparticles by chemical reduction method, *Colloids Surf. A*, 2005, **256**, 111–115.



19 I. G. Koo, M. S. Lee, J. H. Shim, J. H. Ahn and W. M. Lee, Platinum nanoparticles prepared by a plasma-chemical reduction method, *J. Mater. Chem.*, 2005, **15**, 4125.

20 Z. Fan, X. Chen, M. Köhn Serrano, H. Schmalz, S. Rosenfeldt, S. Förster, S. Agarwal and A. Greiner, Polymer Cages as Universal Tools for the Precise Bottom-Up Synthesis of Metal Nanoparticles, *Angew. Chem., Int. Ed.*, 2015, **54**, 14539–14544.

21 X. He, H. Li, Y. Liu, H. Huang, Z. Kang and S.-T. Lee, Water soluble carbon nanoparticles: hydrothermal synthesis and excellent photoluminescence properties, *Colloids Surf., B*, 2011, **87**, 326–332.

22 T. J. Daou, G. Pourroy, S. Bégin-Colin, J. M. Grenèche, C. Ulhaq-Bouillet, P. Legaré, P. Bernhardt, C. Leuvrey and G. Rogez, Hydrothermal Synthesis of Monodisperse Magnetite Nanoparticles, *Chem. Mater.*, 2006, **18**, 4399–4404.

23 H.-C. Chiu and C.-S. Yeh, Hydrothermal Synthesis of SnO_2 Nanoparticles and Their Gas-Sensing of Alcohol, *J. Phys. Chem. C*, 2007, **111**, 7256–7259.

24 S. Vaucher, M. Li and S. Mann, Synthesis of Prussian Blue Nanoparticles and Nanocrystal Superlattices in Reverse Microemulsions, *Angew. Chem., Int. Ed.*, 2000, **39**, 1793–1796.

25 T. Forestier, A. Kaiba, S. Pechev, D. Denux, P. Guionneau, C. Etrillard, N. Daro, E. Freysz and J.-F. Létard, Nanoparticles of $\text{Fe}(\text{NH}_2\text{-trz})_3\text{Br}_2\cdot 3\text{H}_2\text{O}$ ($\text{NH}_2\text{-trz}$ = 2-amino-1,2,4-triazole) prepared by the reverse micelle technique: influence of particle and coherent domain sizes on spin-crossover properties, *Chem.-Eur. J.*, 2009, **15**, 6122–6130.

26 L. Salmon, G. Molnár, D. Zitouni, C. Quintero, C. Bergaud, J.-C. Micheau and A. Bousseksou, A novel approach for fluorescent thermometry and thermal imaging purposes using spin crossover nanoparticles, *J. Mater. Chem.*, 2010, **20**, 5499.

27 Z. Zhang, R. C. Patel, R. Kothari, C. P. Johnson, S. E. Friberg and P. A. Aikens, Stable Silver Clusters and Nanoparticles Prepared in Polyacrylate and Inverse Micellar Solutions, *J. Phys. Chem. B*, 2000, **104**, 1176–1182.

28 X. M. Lin, C. M. Sorensen, K. J. Klabunde and G. C. Hadjipanayis, Temperature Dependence of Morphology and Magnetic Properties of Cobalt Nanoparticles Prepared by an Inverse Micelle Technique, *Langmuir*, 1998, **14**, 7140–7146.

29 J. H. González-Estefan, M. Gonidec, N. Daro, M. Marchivie and G. Chastanet, Extreme downsizing in the surfactant-free synthesis of spin-crossover nanoparticles in a microfluidic flow-focusing junction, *Chem. Commun.*, 2018, **54**, 8040–8043.

30 J. Puigmarti-Luis, Microfluidic platforms: a mainstream technology for the preparation of crystals, *Chem. Soc. Rev.*, 2014, **43**, 2253–2271.

31 S. Marre and K. F. Jensen, Synthesis of micro and nanostructures in microfluidic systems, *Chem. Soc. Rev.*, 2010, **39**, 1183–1202.

32 S. Förster and M. Antonietti, Amphiphilic Block Copolymers in Structure-Controlled Nanomaterial Hybrids, *Adv. Mater.*, 1998, **10**, 195–217.

33 B. Weber, Synthesis of Coordination Polymer Nanoparticles using Self-Assembled Block Copolymers as Template, *Chem.-Eur. J.*, 2017, **23**, 18093–18100.

34 D. Liu, R. C. Huxford and W. Lin, Phosphorescent nanoscale coordination polymers as contrast agents for optical imaging, *Angew. Chem., Int. Ed.*, 2011, **50**, 3696–3700.

35 A. Pramanik and G. Das, Precursory Ag-bipyridine 2D coordination polymer: a new and efficient route for the synthesis of Ag nanoparticles, *CrystEngComm*, 2010, **12**, 401–405.

36 Z. R. Ranjbar and A. Morsali, Sonochemical synthesis of a novel nano-rod two-dimensional zinc(II) coordination polymer; preparation of zinc(II) oxide nanoparticles by direct thermolyses, *Ultrason. Sonochem.*, 2011, **18**, 644–651.

37 J. Larionova, Y. Guari, C. Sangregorio and C. Guérin, Cyano-bridged coordination polymer nanoparticles, *New J. Chem.*, 2009, **33**, 1177.

38 H. Cao, *Synthesis and Applications of Inorganic Nanostructures*, Wiley-VCH Verlag GmbH & Co. KGaA, Weinheim, Germany, 2017.

39 V. Martínez, I. Boldog, A. B. Gaspar, V. Ksenofontov, A. Bhattacharjee, P. Gütlich and J. A. Real, Spin Crossover Phenomenon in Nanocrystals and Nanoparticles of $[\text{Fe}(3\text{-Fpy})_2\text{M}(\text{CN})_4]$ ($\text{M}^{\text{II}} = \text{Ni, Pd, Pt}$) Two-Dimensional Coordination Polymers, *Chem. Mater.*, 2010, **22**, 4271–4281.

40 J. Larionova, L. Salmon, Y. Guari, A. Tokarev, K. Molvinger, G. Molnár and A. Bousseksou, Towards the Ultimate Size Limit of the Memory Effect in Spin-Crossover Solids, *Angew. Chem., Int. Ed.*, 2008, **47**, 8236–8240.

41 Y. Guari, J. Larionova, K. Molvinger, B. Folch and C. Guérin, Magnetic water-soluble cyano-bridged metal coordination nano-polymers, *Chem. Commun.*, 2006, 2613–2615.

42 Y. Guari, J. Larionova, M. Corti, A. Lascialfari, M. Marinone, G. Poletti, K. Molvinger and C. Guérin, Cyano-bridged coordination polymer nanoparticles with high nuclear relaxivity: toward new contrast agents for MRI, *Dalton Trans.*, 2008, 3658–3660.

43 L. Catala, C. Mathonière, A. Gloter, O. Stephan, T. Gacoin, J.-P. Boilot and T. Mallah, Photomagnetic nanorods of the $\text{Mo}(\text{CN})_8\text{Cu}_2$ coordination network, *Chem. Commun.*, 2005, 746–748.

44 T. Uemura and S. Kitagawa, Prussian blue nanoparticles protected by poly(vinylpyrrolidone), *J. Am. Chem. Soc.*, 2003, **125**, 7814–7815.

45 Q. Song, S. K. Nataraj, M. V. Roussenova, J. C. Tan, D. J. Hughes, W. Li, P. Bourgoin, M. A. Alam, A. K. Cheetham, S. A. Al-Muhtaseb and E. Sivaniah, Zeolitic imidazolate framework (ZIF-8) based polymer nanocomposite membranes for gas separation, *Energy Environ. Sci.*, 2012, **5**, 8359.

46 R. Weeber, M. Hermes, A. M. Schmidt and C. Holm, Polymer architecture of magnetic gels: a review, *J. Phys.: Condens. Matter*, 2018, **30**, 63002.

47 S. Reinicke, S. Döhler, S. Tea, M. Krekhova, R. Messing, A. M. Schmidt and H. Schmalz, Magneto-responsive hydrogels based on maghemite/triblock terpolymer hybrid micelles, *Soft Matter*, 2010, **6**, 2760–2773.



48 M. Krekhova, T. Lang, R. Richter and H. Schmalz, Thermoreversible hydroferrogels with tunable mechanical properties utilizing block copolymer mesophases as template, *Langmuir*, 2010, **26**, 19181–19190.

49 O. Eksik, J. Gao, S. A. Shojaee, A. Thomas, P. Chow, S. F. Bartolucci, D. A. Lucca and N. Koratkar, Epoxy nanocomposites with two-dimensional transition metal dichalcogenide additives, *ACS Nano*, 2014, **8**, 5282–5289.

50 J. Gass, P. Poddar, J. Almand, S. Srinath and H. Srikanth, Superparamagnetic Polymer Nanocomposites with Uniform Fe_3O_4 Nanoparticle Dispersions, *Adv. Funct. Mater.*, 2006, **16**, 71–75.

51 J. L. Wilson, P. Poddar, N. A. Frey, H. Srikanth, K. Mohomed, J. P. Harmon, S. Kotha and J. Wachsmuth, Synthesis and magnetic properties of polymer nanocomposites with embedded iron nanoparticles, *J. Appl. Phys.*, 2004, **95**, 1439–1443.

52 J. Li, S. I. Seok, B. Chu, F. Dogan, Q. Zhang and Q. Wang, Nanocomposites of Ferroelectric Polymers with TiO_2 Nanoparticles Exhibiting Significantly Enhanced Electrical Energy Density, *Adv. Mater.*, 2009, **21**, 217–221.

53 J. Schöbel, C. Hils, A. Weckwerth, M. Schlenk, C. Bojer, M. C. A. Stuart, J. Breu, S. Förster, A. Greiner, M. Karg and H. Schmalz, Strategies for the selective loading of patchy worm-like micelles with functional nanoparticles, *Nanoscale*, 2018, **10**, 18257–18268.

54 J. Schöbel, M. Burgard, C. Hils, R. Dersch, M. Dulle, K. Volk, M. Karg, A. Greiner and H. Schmalz, Bottom-Up Meets Top-Down: Patchy Hybrid Nonwovens as an Efficient Catalysis Platform, *Angew. Chem., Int. Ed.*, 2017, **56**, 405–408.

55 J. Schöbel, M. Karg, D. Rosenbach, G. Krauss, A. Greiner and H. Schmalz, Patchy Wormlike Micelles with Tailored Functionality by Crystallization-Driven Self-Assembly: A Versatile Platform for Mesostructured Hybrid Materials, *Macromolecules*, 2016, **49**, 2761–2771.

56 Z. Fan, M. Köhn Serrano, A. Schaper, S. Agarwal and A. Greiner, Polymer/Nanoparticle Hybrid Materials of Precise Dimensions by Size-Exclusive Fishing of Metal Nanoparticles, *Adv. Mater.*, 2015, **27**, 3888–3893.

57 C. Göbel, C. Hils, M. Drechsler, D. Baabe, A. Greiner, H. Schmalz and B. Weber, Confined Crystallization of Spin-Crossover Nanoparticles in Block-Copolymer Micelles, *Angew. Chem., Int. Ed.*, 2020, **59**, 5765–5770.

58 O. Klimm, C. Göbel, S. Rosenfeldt, F. Puchtler, N. Miyajima, K. Marquardt, M. Drechsler, J. Breu, S. Förster and B. Weber, Synthesis of $\text{Fe}(\text{L})(\text{bipy})n$ spin crossover nanoparticles using block copolymer micelles, *Nanoscale*, 2016, **8**, 19058–19065.

59 C. Göbel, O. Klimm, F. Puchtler, S. Rosenfeldt, S. Förster and B. Weber, Synthesis of $[\text{Fe}(\text{L}_{\text{eq}})(\text{L}_{\text{ax}})]_n$ coordination polymer nanoparticles using block copolymer micelles, *Beilstein J. Nanotechnol.*, 2017, **8**, 1318–1327.

60 B. Connerney, P. Jensen, P. E. Kruger, B. Moubaraki and K. S. Murray, Synthesis and structural characterisation of two coordination polymers (molecular ladders) incorporating $[\text{M}(\text{OAc})_2]_2$ secondary building units and 4,4'-bipyridine [$\text{M} = \text{Cu}(\text{n}), \text{Zn}(\text{n})$], *CrystEngComm*, 2003, **5**, 454–458.

61 Y. V. Kokunov, Y. E. Gorbunova, V. V. Kovalev and A. S. Kozyukhin, 2D-layered structure of coordination polymer, zinc trifluoroacetate-1,3-bis(4-pyridyl)propane, *Russ. J. Inorg. Chem.*, 2014, **59**, 187–191.

62 N. Ali and S.-Y. Park, Micellar structures of poly(styrene-*b*-4-vinylpyridine)s in THF/toluene mixtures and their functionalization with gold, *Langmuir*, 2008, **24**, 9279–9285.

63 D. J. Adams and P. D. Topham, in *Supramolecular Chemistry*, ed. P. A. Gale and J. W. Steed, John Wiley & Sons, Ltd, Chichester, UK, 2012.

64 F. Neese, The ORCA program system, *Wiley Interdiscip. Rev.: Comput. Mol. Sci.*, 2012, **2**, 73–78.

65 A. Schäfer, H. Horn and R. Ahlrichs, Fully optimized contracted Gaussian basis sets for atoms Li to Kr, *J. Chem. Phys.*, 1992, **97**, 2571–2577.

66 A. D. Becke, Density-functional exchange-energy approximation with correct asymptotic behavior, *Phys. Rev. A: At., Mol., Opt. Phys.*, 1988, **38**, 3098–3100.

67 S. Grimme, S. Ehrlich and L. Goerigk, Effect of the damping function in dispersion corrected density functional theory, *J. Comput. Chem.*, 2011, **32**, 1456–1465.

68 S. Grimme, J. Antony, S. Ehrlich and H. Krieg, A consistent and accurate *ab initio* parametrization of density functional dispersion correction (DFT-D) for the 94 elements H–Pu, *J. Chem. Phys.*, 2010, **132**, 154104.

69 A. Klamt and G. Schüürmann, COSMO: a new approach to dielectric screening in solvents with explicit expressions for the screening energy and its gradient, *J. Chem. Soc., Perkin Trans. 2*, 1993, 799–805.

70 I. V. Morozov, E. V. Karpova, T. Y. Glazunova, A. I. Boltalin, M. A. Zakharov, D. S. Tereshchenko, A. A. Fedorova and S. I. Troyanov, Trifluoroacetate complexes of 3d elements: Specific features of syntheses and structures, *Russ. J. Coord. Chem.*, 2016, **42**, 647–661.

